Effects of decimetre-scale surface roughness on L-band Brightness Temperature of Sea Ice

Maciej Miernecki[2,1], Lars Kaleschke[3,1], Nina Maaß[1], Stefan Hendricks[3], and Sten Schmidl Søbjrg[4]

[1]Institute of Oceanography (IfM), University of Hamburg, Bundesstr. 53, 20146 Hamburg Germany
[2]Centre d'Etudes Spatiales de la Biosphère (CESBIO), 18 avenue Edouard Belin bpi 2801, 31401 Toulouse Cedex 9, France
[3]Alfred Wegener Institute, Helmholtz Centre for Polar and Marine Research, Bremerhaven, Bussestrasse 24, 27570 Bremerhaven, Germany
[4]Technical University of Denmark, Ørsteds Plads, 2800 Kgs. Lyngby Danmark

Correspondence: Maciej Miernecki (maciej.miernecki@cesbio.cnes.fr)

Abstract. Sea ice thickness measurements with L-band radiometry is a technique which allows daily, weather-independent monitoring of the polar sea ice cover. The sea-ice thickness retrieval algorithms relay on the sensitivity of the L-band brightness temperature to sea-ice thickness. In this work, we investigate the decimetre-scale surface roughness as a factor influencing the L-band emissions from sea ice. We used an airborne laser scanner to construct a digital elevation model of the sea ice surface.

5   We found that the probability density function of surface slopes is exponential for a range of degrees of roughness. Then we applied the geometrical optics, bounded with the MIcrowave L-band LAyered Sea ice emission model in the Monte Carlo simulation to simulate the effects of surface roughness. According to this simulations, the most affected by surface roughness is the vertical polarization around Brewster's angle, where the decrease in brightness temperature can reach 8K. The vertical polarization for the same configuration exhibits a 4K increase. The near-nadir angles are little affected, up to 2.6K decrease

10 for the most deformed ice. Overall the effects of large-scale surface roughness can be expressed as a superposition of two factors: the change in intensity and the polarization mixing. The first factor depends on surface permittivity, second shows little dependence on it. Comparison of the brightness temperature simulations with the radiometer data does not yield definite results.

1 Introduction

The L-band brightness temperature (T_B) is sensitive to sea ice thickness, a feature that is used for sea ice thickness retrieval from L-band T_B (over thin ice, <1.5m) Tian-Kunze et al. (2014), Huntemann et al. (2014), Kaleschke et al. (2016). Several factors influence the T_B measured over ice-covered regions: ice concentration, ice temperature, snow cover and surface roughness are among them Maaß et al. (2013), Ulaby et al. (2014). Here, we investigate the effect of surface roughness on the L-band T_B, a

20 factor that so far has not been included in the modeling of the sea ice emissions and in operational sea ice thickness retrieval.

In the theory of electromagnetic scattering, the roughness of a random surface is characterized by statistical parameters such as the standard deviation of surface height (σ_z), and the correlation function ($R(\xi)$) measured in units of wavelength Ulaby et al. (2014). The measurements of surface elevation (z), from which the roughness statistics are drawn, are conducted with altimeters characterized by their accuracy (δ) and sampling distance (Δx). Thus, the measurement method has an impact on the

5   result by filtering out spatial frequencies of the surface roughness. The sea ice elevation measurements obtained from air-borne altimeters Ketchum (1971), Dierking (1995), supplemented with terrestrial laser scanners Landy et al. (2015), draw a picture of sea ice roughness as a multi-scale feature covering several orders of magnitude from large floes and pressure ridges of tens and hundreds meters to frost flowers and small ripples of centimeters to millimeters scales. The incident wavelength reacts differently with individual components of the superimposed roughness Ulaby et al. (2014). The roughness scales much greater

10   than the electromagnetic wavelength (λ) alter the local incidence angle. On the other end of the roughness spectrum, when the change of the surface elevation Δz across sampling distance Δx is much smaller than λ, the roughness stays unnoticed. As a rule of thumb, the Δx should be smaller than 0.1λ Dierking (2000). Sea ice roughness measurements with terrestrial lidar carried out by Landy et al. (2015) show that σ_z ranges from 0.10cm to 0.64cm, after high-pass filtering (cut off at 0.25m, Δx = 2mm). These results indicate that, according to the Fraunhofer's smoothness criterion, most sea ice types (except artificially

15   grown frost flowers), can be treated as a smooth surface for L-band at scales lower than 0.25m. In this study we will focus on the other side of the roughness spectrum; the large-scale surface roughness of sea ice. Studies of surface scattering with numerical simulations conclude that a region of $8\lambda \times 8\lambda$ is large enough to represent small-scale surface roughness in scattering models Lawrence et al. (2011), Lawrence et al. (2013). Hereby we assume that scales greater than 8λ the surface roughness can be characterized in terms of geometrical optics (GO). In GO the surface is represented as a set of facets Ulaby et al. (2014). This

20   approach was applied in modeling of the effective emissivities of mountainous terrain Matzler and Standley (2000), as well as other surfaces such as the one of the sea Prigent and Abba (1990). The latter study involved probability distribution of slopes in across- and downwind directions. A similar method was used in the context of sea ice to assess the uncertainties caused by the roughness in sea ice concentration products derived from passive microwaves Stroeve et al. (2006). (Liu et al., 2014) measured ice surface slopes and other roughness statistics in the Bohai Sea, but their result was obtained with linear (1-D) scans under the

25   assumption of isotropic roughness characteristics. The study by (Beckers et al., 2015) has demonstrated that the statistics of sea ice roughness (mean z, σ_z, kurtosis and skewness) obtained from 1-D altimeter and 2-D laser scanner converge, provided that the surface is not strongly heterogeneous. Nonetheless, the 1-D altimeter data cannot properly represent the spatial orientation of surface facets, which orientation is characterized by both the slope (α) and the azimuthal angle in which it is facing (γ). In this work, we address the issue of surface slope orientation by extracting this information from the digital elevation model

30   (DEM) obtained with 2-D measurements. Then we identify the spatial scales at which sea ice can be treated as isotropic in terms of surface slopes orientation. The surface roughness statistics are subsequently used in combination with the MIcrowave L-band LAyered Sea ice emission model (MILLAS) to simulate the brightness temperature over ice with different degrees of roughness. Finally, we compare the EMIRAD-2 radiometer measurements with modeled T_B with and without roughness parametrization.

2 Materials and Methods

The SMOSice2014 campaign took place between March 21, 2014 and March 27, 2014 in the area between Edgeøya and Kong Karls Land, east of Svalbard. A broader description of the campaign was made by (Kaleschke et al., 2016),(Hendricks et al., 2014). In this study we analyzed the data acquired during the flights on March 24/26, at this point, we evoke just the parts
5 relevant to the presented work.

2.1 SMOSice2014 Campaign

In the period preceding the experiment, from late January until early March, the meteorological conditions in the region deviated strongly from the climatological means. The air temperature measured at Hopen Island meteorological station was on average 9 to 12°C higher than the climatological value for the period 1961-1990 Strübing and Schwarz (2014). Prevailing
10 southerly winds pushed sea ice against the coasts of Nordaustlandet and into Hinlopen Strait, leaving a small strip of compacted ice along the coasts of Edgeøya. When sea ice returned with southerly drift in early March it set the scene for the experiment. The thickest, most deformed ice was located in the western part of the studied region with a gradual decrease in thickness eastwards, where thin newly-formed ice was dominant. This pattern can be observed in the SMOS sea ice thickness product displayed in Figure 1a. In this work, we analyze only the data from the low altitude flight at 70m, as it has the highest spatial
15 resolution of the Airborne Laser Scanner (ALS) among all the flights. Also, we limit the analysis to the 24th of March, it is due to the fact that the region covered on 26th March had a discontinuous ice cover and a large scale swell was interfering with the surface elevation measurements. On March 24, the Polar 5 research aircraft of the Alfred Wegener Institute (Bremerhaven, Germany), undertook measurement flights starting from the eastern coast of Edgeøya, along the lines marked in red and green on Figure 1b. The figure also shows TerraSAR wide swath scenes, taken in the region. Flight A was made between 10:05 and
20 10:41 UTC, flight B from 11:25 to 12:07 UTC. A set of instruments was mounted on the aircraft, including an aerial camera to visually register the ice conditions, the Heitronics KT19.85 pyrometer for surface temperature measurements, the L-band radiometer EMIRAD-2 and the Airborne Laser Scanner for high-resolution surface elevation measurements.

2.2 EMIRAD-2 Radiometer

The EMIRAD-2 L-band radiometer, developed by DTUSpace, is a fully polarimetric system with advanced radio frequency
25 interference (RFI) detection features Søbjaerg et al. (2013). The setup mounted on the aircraft consists of two Potter horn antennas, one nadir pointing, one side looking at 45°incidence angle. The antennas footprints dimensions for a 70m flight altitude are approximately 60m and 70m by 90m, respectively. The receiver has a sensitivity of 0.1K for 1s integration time. During all flight operations navigation data are collected and used to transform the polarimetric brightness temperature into the Earth reference frame Hendricks et al. (2014). The EMIRAD-2 data have been screened by evaluating kurtosis, polarimetric
30 Balling et al. (2012), and brightness temperature (T_B) anomalies, this revealed up to 30% RFI contamination. When subtracting the mean value of the RFI-flagged data from the mean value of the full data a difference of typically a few Kelvin is present for a side looking horn and typically 10K for the nadir-looking horn. Data analysis further revealed a 20K offset relative to the
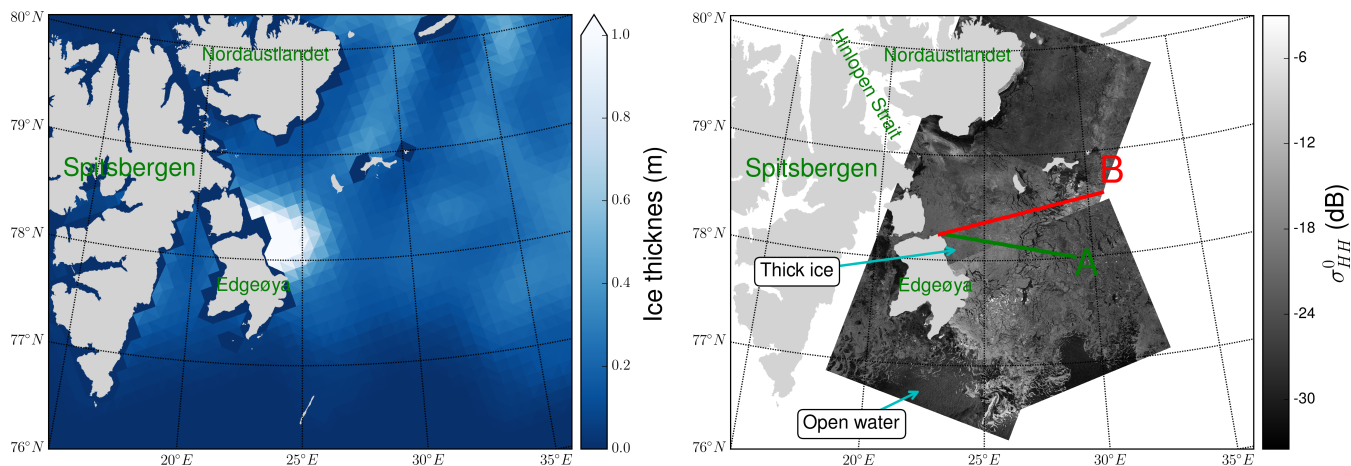
(a) Sea ice thickness on March 24 2014, derived from SMOS. The SMOS sea ice thickness product with a resolution of 40km is presented on 15km grid. An aggregation of thick ice (>1m) is visible along the Edgeoya's eastern coast.

(b) Sea ice conditions in the flights region on March 24. The TerraSAR-X wide swath mode (HH polarization), with frames taken at 05:35 UTC and 14:58 UTC. The aircraft tracks are marked in green - A at 10:05-10:41 UTC and red - B at 11:25-12:07 UTC.

Figure 1. The region of SMOSice2014 Campaign.

nadir vertical channel caused by a continuous wave signal from the camera that was mounted on the airplane to obtain visual images. This contamination could not be detected by the RFI filters but the analysis concludes a purely additive characteristic and allowed a bias correction Hendricks et al. (2014). In this study, we use the data pre-processed by the DTU-team. The radiometer data was RFI cleaned and bias-corrected and validated using aircraft wing wags and nose wags over open ocean

5   Hendricks et al. (2014).

2.3   Airborne Laser Scanner

The Riegel VQ-580 laser scanner is essential to this study, as it is used for measuring the surface elevation from which sea ice thickness is estimated, as well as the surface topography characterized. The near-infrared laser (wavelength 1064nm) is measuring snow and ice elevation with the accuracy and precision of 25mm. During the flights it was operating with pulse

10   repetition frequency of 50kHz, measuring the surface elevation in cross track linear scan in the range of ±30 degrees. Such configuration at the flight altitude of 70m resulted in across-track and along track sampling of 25cm and 50cm, respectively. The data were calibrated and geo-referenced to the WGS84 datum. Further processing involved manual classification of tie points in leads in order to obtain the local sea level and sea ice free-board Hendricks et al. (2014). The geo-referenced surface elevations are used to compute surface roughness statistics. The elevation data are interpolated to a regular 0.5m by 0.5m

15   grid to form a digital elevation model (DEM) of the sea ice surface. The DEM serves to derive surface slopes orientation. The ALS free-board data is used to estimate the sea ice thickness. The estimation method uses the assumption of hydro-static equilibrium. In order to derive the sea ice thickness, the densities of water and ice must be known, as well as the snow load,

described by snow density and snow thickness. Unfortunately, during the flights the snow radar was still in the test phase of development, therefore we decided not to use this data. In order to tackle the problem of the lack of the snow thickness data, we follow (Kaleschke et al., 2016) and assume an approximation formula used by (Yu and Rothrock, 1996) and (Mäkynen et al., 2013), which sets the snow thickness to 10% of the sea ice thickness. As for the respective densities, we assume the water

5   density as 1027kg/m^3, ice density 917kg/m^3 after (Ricker et al., 2014) and snow density 300kg/m^3 after (Warren et al., 1999).

2.4   Sea Ice Brightness Temperature Simulation

For the simulation of sea ice brightness temperature (T_B) we use the MIcrowave L-band LAyered Sea ice emission model described by (Maaß et al., 2013), further referred to as MILLAS. This model is based on the radiative transfer model of (Burke et al., 1979)(who used it for soils), with infinite half-space of seawater covered with layers of sea ice, snow and a top semi-

10   infinite layer of air. In contrast to the original model of (Burke et al., 1979) and its usage by (Maaß et al., 2013), the current version of MILLAS takes into account multiple reflections at the layer boundaries. The MILLAS model describes the brightness temperature above snow-covered sea ice as a function of temperature and permittivity of the layers. The water permittivity depends mainly on the water temperature and salinity Klein and Swift (1977). Ice permittivity can be approximately described as a function of brine volume fraction Vant et al. (1978), which depends on ice salinity and the densities of the ice and brine

15   Cox and Weeks (1982), which in turn depend mainly on ice temperature. The permittivity of dry snow can be estimated from its density and temperature Tiuri et al. (1984). In the simulation setup, the ice and water salinity are kept constant. Furthermore, we assume that the system is in thermal equilibrium, and the water beneath the ice is at the freezing point. In this configuration, the T_B is simulated as a function of ice thickness (d_{ice}), snow thickness (d_{snow}) and surface temperature (T_{surf}). In our setup, the snow is assumed to be dry with a density of 300kg/m^3 , which is the average snow density value for December Arctic

20   measurements from 1954-91 Warren et al. (1999). The TB simulations are only slightly sensitive to snow density, see Figure 3 in (Maaß et al., 2013). The permittivities of snow and ice are linked to their temperature. The temperature profiles within snow and ice are assumed to be continuous and linear. The values for the ice and snow thermal conductivity are taken from (Yu and Rothrock, 1996), (Untersteiner, 1961). As the optimization of the emission model lays boned the scope of this work, we use the simplest setup variant of the MILLAS model consisting of a single layer of ice covered with a single layer of snow.

25   ### 2.5   Sea Ice Surface Roughness

We used the ALS data from SMOSice2014 to measure the decimeter-scale surface roughness. In the context of the radiation transfer, the surface roughness is characterized in relation to incident wavelength. The ALS spatial resolution of 0.5m is a few times larger than the L-band wavelength in sea ice ($\lambda_{ice} = \lambda/\sqrt{\epsilon_{ice}} \approx 0.12$m), which makes it suitable to measure the large-scale roughness, the part of the roughness spectrum where geometrical optics can be used to approximate the path of

30   radiation. In the first step, we identify the ice with different degree of surface roughness. For that, we divide the flight tracks into one-second sections (approximately 70 m long), large enough to cover the entire nadir radiometer footprint, and we make a histogram of the standard deviations of surface heights computed from these sections. The number of bins in the histogram is set according to the formula: $N_{bins} = 5\log_{10}(N_{data})$, after Panofsky Hans A. and Brier Glenn W. (1958). We decided on

standard deviation as the criterion for defining the roughness classes, as it is widely used to characterize surface roughness from elevation profiles, and unlike visual interpretation of the aerial photography of sea ice it does not introduce personal biases. The resulting histogram in Figure 2, shows the sea ice roughness classes as histograms bins. No strips within the lowest standard deviation of surface height were found, that is probably due to the fact that no refrozen lead of the scale of 70m was found or the ALS laser signal was not reflected back from the surface resulting in a missing data.
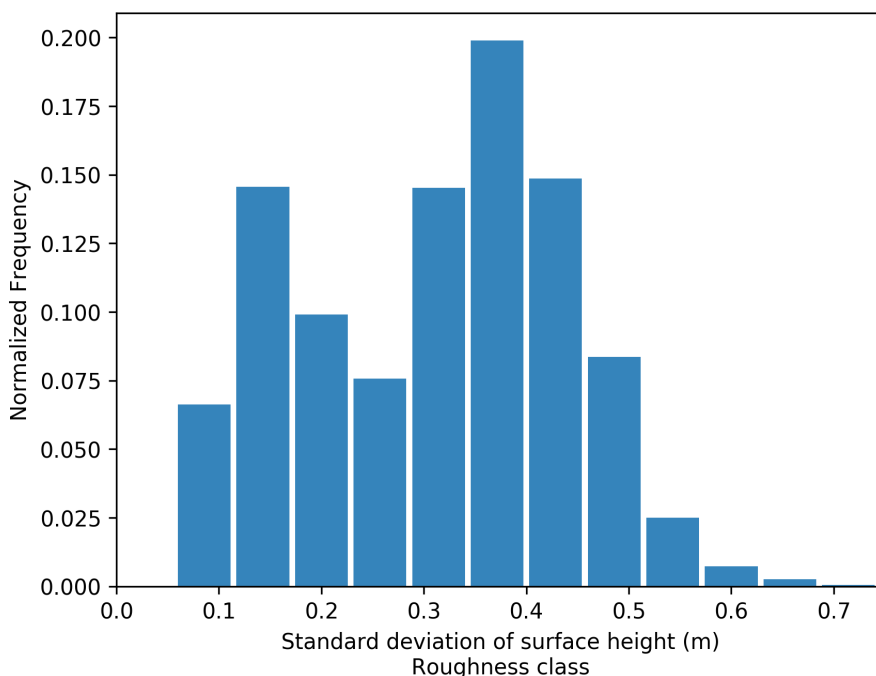
Figure 2. Histogram of the standard deviation of surface heights computed from 70m flight strips, bins define the roughness classes of sea ice.

In the second step, we interpolate the ALS elevation measurements to a regular 0.5m grid in order to form a digital elevation model (DEM) of the sea ice surface. The sea ice surface in the DEM is represented as a set of triangular facets. Each facet orientation in the 3D Cartesian space (For simplicity we assume the base vectors $\hat{x}, \hat{y}, \hat{z}$ to be aligned with the aircraft principal axis, so the $\hat{x}$ points to the flight direction), is described by two angles: the facet slope α ($0 \leq \alpha < \pi$) and the facet azimuthal direction γ (-$\pi \leq \gamma < \pi$). Therefore, the i-th facet local normal vector is described by:

$$\hat{n}_i = -\hat{x}\sin(\alpha_i)\cos(\gamma_i) - \hat{y}\sin(\gamma_i)\sin(\alpha_i) + \hat{z}\cos(\alpha_i) \tag{1}$$

In the third step, we compute the normal vectors and their orientations for the individual facets. This is done for all roughness classes. We found that the azimuthal orientation angle γ does not show any preferred directions within any given roughness class. Local elongated structures such as pressure ridges along the cost have dominant directions of the slopes, however, our

study concluded that in the entire region, the distribution of azimuthal orientation angle γ is isotropic at scales greater than 4.3km (Not shown). Therefore for the purpose of this study, we assume the distribution of to be random and isotropic. As far as the facet slope is concerned, for all roughness classes we observe a similar probability density (PDF) with a maximum at zero and a gradual decline in the likelihood of encountering the steeper slopes. Figure 3 shows the PDF_α in a logarithmic

5 scale for the three distinct roughness classes: smooth $0.05m < \sigma_z < 0.11m$ (in blue), medium rough $0.28m < \sigma_z < 0.34m$ (in green) and rough $0.45m < \sigma_z < 0.51m$ (in red).
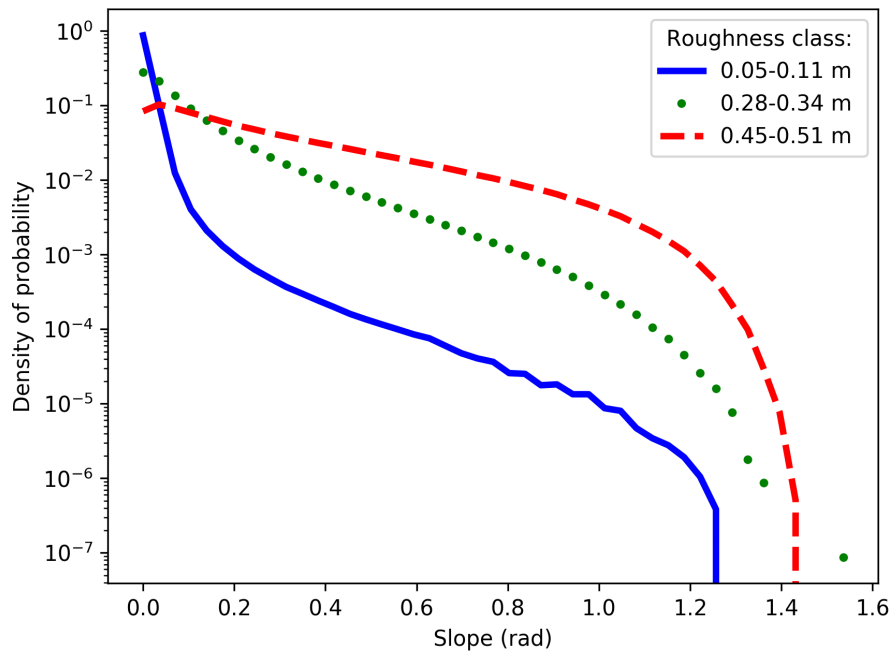
Figure 3. Density of probability of surface slopes in logarithmic scale for three roughness classes: smooth $0.05m < \sigma_z < 0.11m$ (in blue), medium rough $0.28m < \sigma_z < 0.34m$ (in green) and rough $0.45m < \sigma_z < 0.51m$ (in red)

We decide to approximate the PDF of surface slopes with an exponential curve:

$$PDF_\alpha = A \exp((\alpha/s_\alpha)), \tag{2}$$

where A is the normalization constant and s_α is the "geometrical-slope roughness parameter". For some roughness classes

10 other functions can be fitted more accurately, however the exponential function performs well in all roughness classes and because it is a one-parameter function (with s_α defining it's shape), it is strait forward to interpret in terms of roughness - PDF_α relation. Figure 4 shows the relation between s_α and the standard deviation of surface heights corresponding to the roughness classes defined above. The error bars manifest the uncertainty associated with each data point. The large uncertainty for the very rough ice is caused by a relatively small number of data samples from such regions. The quadratic relation

is holding well for ice with up to 0.5m standard deviation of surface heights. The red dashed line marks the fitted curve:
$$s_\alpha = 0.9009\sigma_z^2 + 0.0263\sigma_z + 0.0024$$
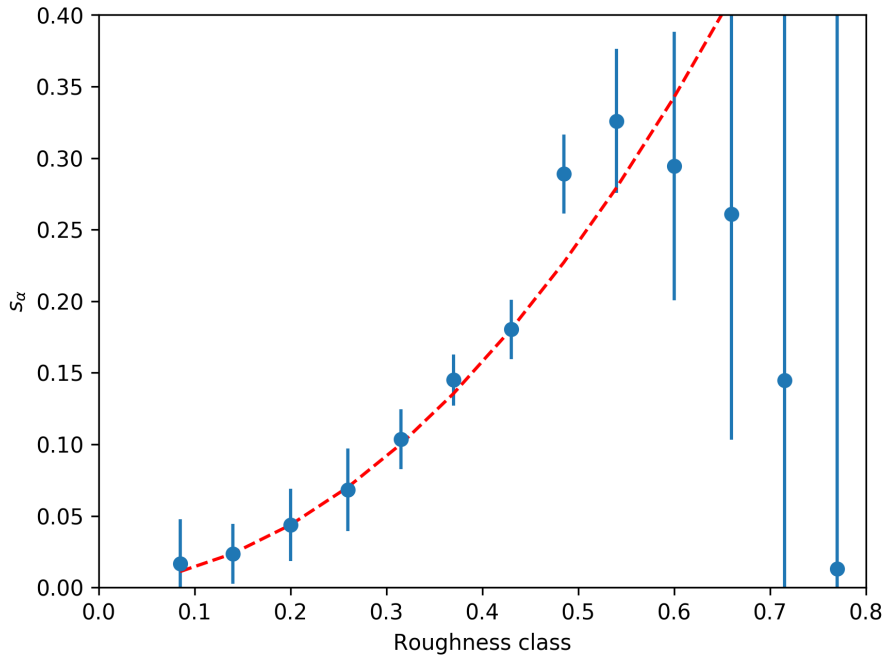
Figure 4. Surface roughness parameter s_α describing the probability distribution of surface slopes. Error bars are proportional to the uncertainties, Inverse of the number of data points in each roughness class.

2.6 Simulation of Brightness Temperature of Rough Sea Ice

In the previous section, we described the sea ice surface as composed of facets with orientation described by two angles:
the slope α and the azimuthal direction γ. Subsequently, we analyzed the ALS data to extract information about statistical distributions of slopes and their orientation. Finally, we conclude that the exponential function is suitable to describe the probability density function of surface slopes for a range of ice surfaces with different degree of surface roughness. In this section, we describe how we integrate the probability description of faceted sea ice surface with the MILLAS emission model. To start, let's evoke the "global" coordination system in cartesian basis $(\hat{x}, \hat{y}, \hat{z})$ in which the radiometer antenna-look direction $(\hat{r})$ is described as:

$$\hat{r} = \hat{x}\sin(\theta_0)\cos(\phi_0) + \hat{y}\sin(\theta_0)\sin(\phi_0)\hat{z}\cos(\theta_0), \tag{3}$$

where the θ_0 is the antenna incidence angle and the ϕ_0 is the azimuthal direction of the antenna. The antenna setting defines the directions of the horizontal ($\hat{h}$) and vertical ($\hat{v}$) polarization vectors:

$$\hat{h} = -\hat{x}\sin(\phi_0) + \hat{y}\cos(\phi_0), \qquad \hat{v} = -\hat{x}\cos(\theta_0)\cos(\phi_0) - \hat{y}\cos(\theta_0)\sin(\phi_0) - \hat{z}\sin(\theta_0). \tag{4}$$

In order to unravel the relation between the radiation originating from a tilted face of the facet and the flat one, we must
5   consider the "local" coordinate system associated with *i*-th facet (variables associated with individual facets are denoted with subscript *i*). The local z-coordinate is aligned with the facet normal vector $\hat{n}_i$, followed by $\hat{x}_i$ and $\hat{y}_i$ calculated accordingly:

$$\hat{z}_i = \hat{n}_i \qquad \hat{y}_i = \frac{\hat{n}_i \times \hat{r}}{|\hat{n}_i \times \hat{r}|} \qquad \hat{x}_i = \hat{y}_i \times \hat{z}_i \tag{5}$$

The local incidence angle θ_i is therefore calculated as :

$$\theta_i = \cos^{-1}(-\hat{r} \cdot \hat{n}_i) \tag{6}$$

10   Thus the local horizontal and vertical polarization vector are not aligned with the global ones:

$$\hat{h}_i = \hat{y}_i, \qquad \hat{v}_i = -\hat{x}_i\cos(\theta_i) - \hat{z}_i\sin(\theta_i) \tag{7}$$

The emissions from the facet at an angle θ_i and polarization p are denoted with an asterisk: $T_B^*(\theta_i; p)$. In order to calculate the brightness temperatures observed in the global horizontal and vertical polarization it is necessary to account for the coordinates rotation (Ulaby et al., 2014):

15   $$T_{Bi}(\theta_i; H) = (\hat{h} \cdot \hat{h}_i)^2 T_B^*(\theta_i; H) + (\hat{h} \cdot \hat{v}_i)^2 T_B^*(\theta_i; V) \tag{8a}$$

$$T_{Bi}(\theta_i; V) = (\hat{v} \cdot \hat{h}_i)^2 T_B^*(\theta_i; H) + (\hat{v} \cdot \hat{v}_i)^2 T_B^*(\theta_i; V) \tag{8b}$$

We model the sea ice surface as a set of facets, therefore the brightness temperature registered at the antenna aperture is a sum of contributions from N facets. We assume that each facet is visible at the incidence angle θ_i and covers a patch of antenna
20   field of view equal to the solid angle Ω_i:

$$\Omega_i = \frac{A\cos(\theta_i)}{R^2 \cos(\alpha_i)} \tag{9}$$

The formula summing the contributions from N visible facets also includes the antenna gain component ω_i:

$$T_B(\theta_0; p) = \frac{1}{N\cos(\theta_0)} \sum_{i=1}^{N} \omega_i T_{Bi}(\theta_i; p)\Omega_i \qquad (10)$$

In this stage of our study we aim at modeling the surface roughness effect and for simplicity we assume a constant antenna gain across the whole field of view. We also assume that the antenna is in a far field so the incidence θ_0 is assumed constant

5 across the field of view. These assumptions yield the final formula that was implemented in the geometrical roughness model:

$$T_B(\theta_0; p) = \frac{1}{N\cos(\theta_0)} \sum_{i=1}^{N} T_{Bi}(\theta_i; p)\sec(\alpha_i)(-\hat{r} \cdot \hat{n}_i) \qquad (11)$$

Figure 5 presents the data flow in the Geometrical Roughness Model that is used in modelling the emissions from rough sea ice surface. The model merges the emission model, in this case it is the MILLAS model suitable for sea ice, with the geometrical characterization of the faceted surface. The MILLAS emission model in the presented setup uses the sea ice

10 surface temperature ($T_{surface}$) sea ice thickness (d_{ice}) and snow thickness (d_{snow}) as input variables. The geometrical optics part needs the cumulative probability distribution of surface slopes (CDF_α) and the antenna look direction ($\hat{r}$). The orientation of N facets representing the sea ice surface is calculated with the inverse transform sampling (ITS) Devroye (2006). This method returns a random slope value from a given non-uniform distribution, described by the geometrical roughness parameter s_α. Similarly, the azimuthal angle γ_i is drawn from a uniform distribution. The result of this processing step is the set of N

15 pairs of angles (α_i, γ_i) describing the orientation of N facets. In the next step, the local normal vector and the local incidence angle (θ_i) are calculated for each of the N facets. The θ_i is used for calculating the brightness temperature emitted from the i-th facet with the emission model. The $\hat{r}$ and the $\hat{n}_i$ are used to calculate the local and global polarization directions, as well as the Ω_i. For the final step, the contributions from N facets are summed as in the equation 11. The result is the brightness temperature of the surface observed under θ_0 and polarization p.
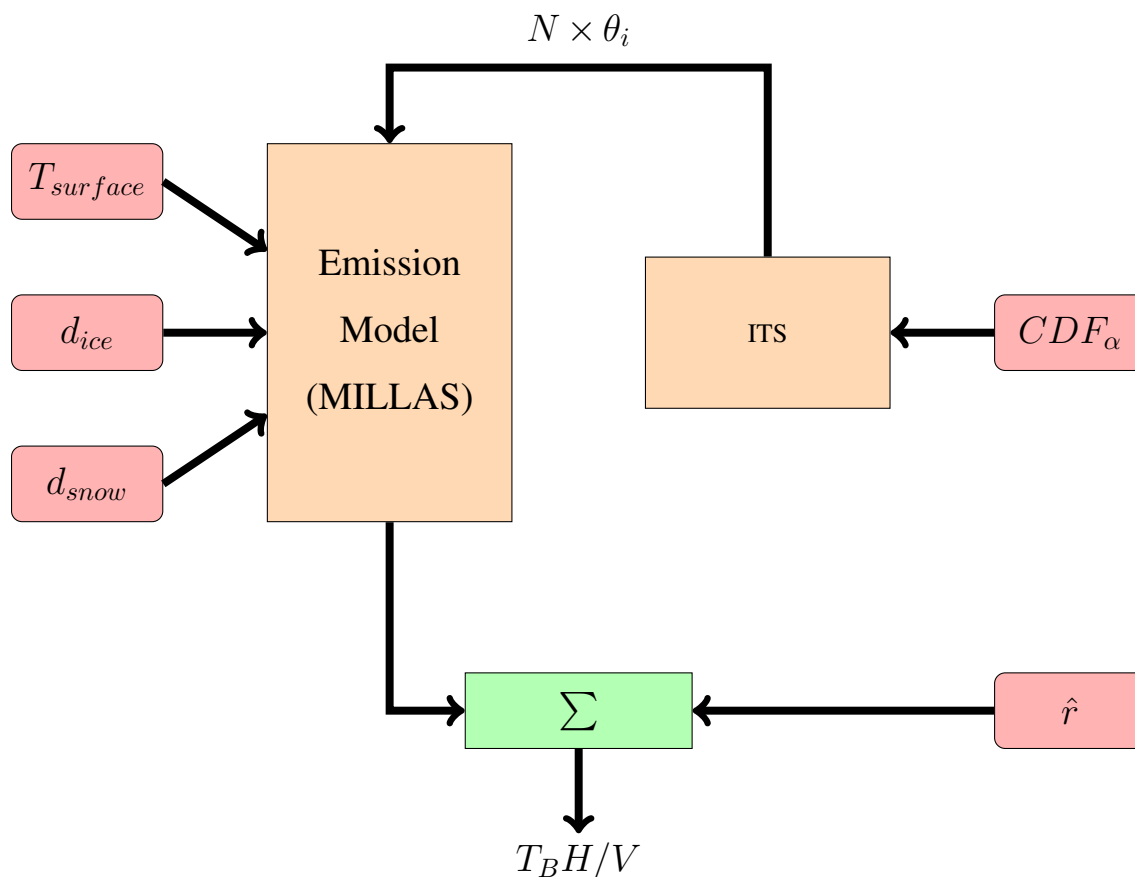
Figure 5. Flowchart showing the processing chain within the geometrical roughness model. Input parameters: $T_{surface}, d_{ice}, d_{snow}, CDF_{\alpha}$, $\hat{r}$.

The number of facets N is an adjustable parameter of the model. For the simulation results to be accurate and repeatable the value of N must be high enough, this however involves a trade-off with the computation time. In order to set the value of N we looked at the standard deviation of 20 simulations for nadir and 45 degrees. We decided that the standard deviation of T_B should be lower than $0.1K$, as this is the accuracy of the EMIRAD-2 radiometer for the one second integration time. This criterion is met for N greater than 10^4, which we take as the N value for further simulations.

3 Results

3.1 Brightness temperature simulations

In this section, we present the results of the brightness temperature simulations for sea ice with different degree of large-scale surface roughness. The degree of roughness is parametrized by the probability distribution of surface slopes described by the

s_α parameter. In our simulation s_α varies between 0.05 and 0.35, which is in accordance with the measurements of surface slopes done during the SMOSice2014. As the aim of this study is to single out the effect of surface roughness, we keep the other parameter in the emissivity model: surface temperature and ice and snow thickness constant ($T_{surface}$ =260K, d_{ice} =1.42m, d_{snow} =0.14m). Further in this section, we will discuss the usage of other emissivity models. The brightness temperatures

5 are calculated for every degree of incidence angle in range 0-70 degrees. Figure 6 shows the simulation results. Dashed lines mark the emissions from the specular surface, whereas the red and blue curves mark the emissions simulated from sea ice with different degree of surface roughness for vertical and horizontal polarizations, respectively. The intensity of the colour of the line corresponds to the roughness parameter used in the simulation.
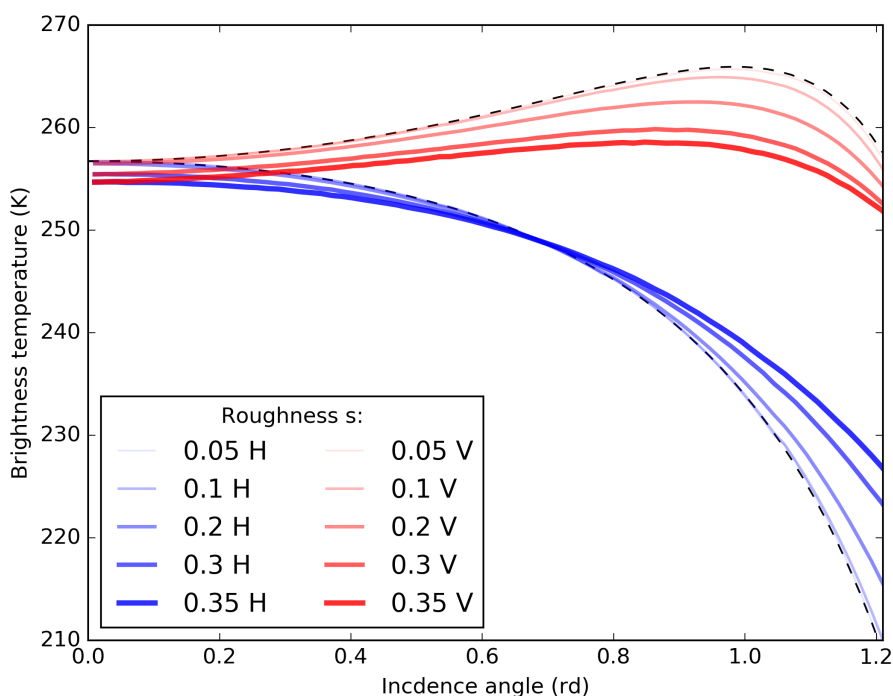
Figure 6. Effects of the large-scale surface roughness on the brightness temperature of sea ice, simulated with geometrical roughness model. Vertical polarization in red, horizontal in blue. The black dashed lines mark the T_B for the specular surface. The surface roughness parameter s_α varies between 0.05 to 0.35, the thicker the line the higher the s_α. The inputs for the MILLAS emissivity model are kept constant: $T_{surface}$=260K, $dice$ =1.42m, d_{snow} =0.14m

The effect of increasing surface roughness is two-fold. First, the polarization difference decreases as the horizontal end

10 vertical polarization curves are brought together. Second, is the overall near-nadir intensity is lowered by 2.6K. The effect of roughness is more visible at higher incidence angles (60°). For the highest value of the roughness parameter, vertical polarization decreases 8K, horizontal polarization experience a 4K increase. The effect of roughness is more pronounced for the higher values of roughness parameter s_α. This fact can be explained by the approach used in this study. High values of s_α

increase the likelihood of encountering a large incidence angles in the inverse transform sampling. The polarization difference for these large incidence angles is larger than for the near-nadir ones, and the curve for vertical polarization is not monotonic. After accounting for polarization rotation, in the summation over N facets, these height incidence angles are contributing more to the overall lowering of the T_B. The two effects: the polarization mixing and the lowering of brightness temperature, can be parametrized in a fashion similar to the HQ model proposed by (Choudhury et al., 1979). Here we propose a formulation with two parameters the H_α and Q_α.

$$T_B(\theta;p) = [(1 - Q_\alpha) \cdot T_B^*(\theta;p) + Q_\alpha T_B^*(\theta;q)] \cdot H_\alpha \tag{12}$$

The H_α accounts for the change in total intensity and the Q_α for the polarization mixing. The emissions from the specular surface are denoted with an asterisk: $T_B^*(\theta;p/q)$. The proposed parametrization approximates the results obtained with the Monte Carlo simulation with a root mean square difference of 0.45K

$$H_\alpha = a_1 s_\alpha^2 + a_0 \qquad\qquad Q_\alpha = b_1 s_\alpha^2 + b_0 \tag{13}$$

where $a_1 = 0.020 \times 10^3$, $a_0 = 1$ and $b_1 = 0.537 \times 10^3$, $b_0 = 0$.

The emissions from the specular surface are an essential input for the geometrical roughness model used in this study. The exact shape of the simulated brightness temperature curves depends on the probability distribution of slopes, as well as on the emission characteristics of the specular surface. In this paragraph, we will investigate how the shape of the $T_B^*(\theta;p/q)$ influences the geometrical roughness model results. The shapes of the polarization curves i.e. the reflectivities for a given incidence angle, are described by Fresnel equations. Equations that are determined by the permittivity of the medium (ϵ). (In this work we omit the question of penetration depth assuming the emissions are coming from the isothermal surface layer.) To investigate the impact of the varying ϵ we take a range of permittivities specific to sea ice, as calculated within the MILLAS model, as well as much higher partitivity corresponding to soil (30.6% sand, 55.9% silt, 13.5% clay) with different water content according to the model of (Mironov et al., 2015). These permittivities are used with the geometrical roughness model to simulate surfaces with different degree of surface roughness, described by s_α. Figures 7,8, show the values of H_α and Q_α as a function of the surface roughness for a range of surface permitivities. The sea ice permitivities from the MILLAS model range between $\epsilon = 3.1 + 0.05i$ (for T_{ice} =271K, S_{ice} =7g/kg) and $\epsilon = 4.6 + 0.8i$ (for T_{ice} =253K, S_{ice} =1g/kg), where T_{ice} is the bulk ice temperature and S_{ice} the bulk ice salinity. The curves corresponding to those values lie close together indicating that the proposed parametrization is suitable to all types of first year sea ice. As the permitivities are getting larger they affect the intensity parameter H_α. The H_α is close to 1 for $\epsilon \approx 19$, pass this value the H_α changes sign which corresponds to increase in $T_B(\theta;p/q)$. The effect of permittivity on the polarization mixing parameter (Q_α) is less pronounced. The dependence of the Q_α parameter on the roughness follows a similar quadratic curve regardless of the surface permittivity. It is important to remind that all those results were obtained with the surface slopes distribution derived from the ALS measurements specific to the different types of sea ice.
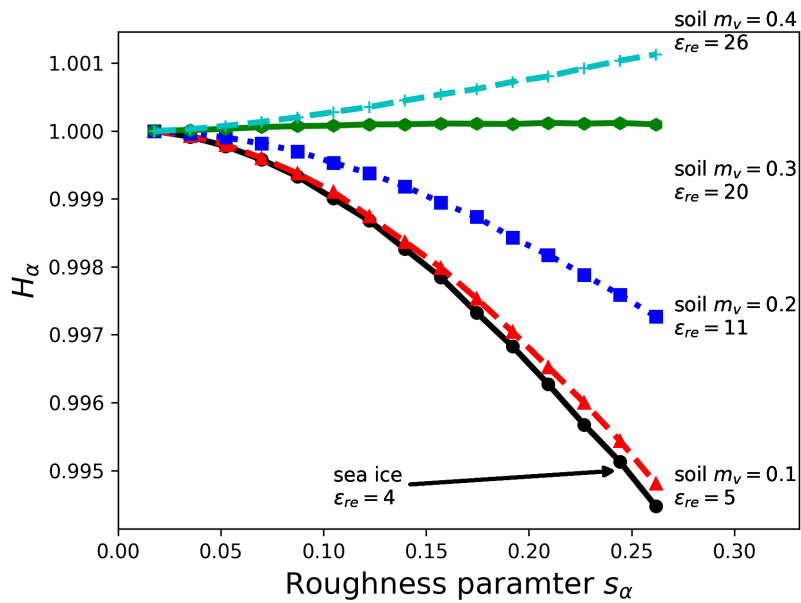
Figure 7. Change in the intensity parameter (H_α) as a function of the roughness parameter s_α. Curves corresponding to different surfaces with different ϵ specific to the water content m_v, are marked in colours.

Figure 8. Change in the polarization mixing parameter (Q_α) as a function of the roughness parameter s_α. Curves corresponding to different surfaces with different specific to the water content m_v, are marked in colours.

3.2 Simulations vs. Measurements

In this section, we compare the brightness temperature measured with the EMIRAD-2 radiometer with brightness temperature simulations. We want to determine simulation setup that is best in reproducing the radiometer measurements. And whether the inclusion of the surface roughness in simulation brings significant improvement. The limitation of this approach is that

5   we assume the ice observed by side looking antenna and the ice below the flight path have the same properties. We consider the surface temperature, the sea ice thickness and the surface roughness along the flight and we use them to run the statistical roughness model, described earlier with a MILLAS single ice layer setup as the brightness temperature module. When needed the snow thickness is set to be 10% of the sea ice thickness. The calculation is done for 60s averages, during which the aircraft covers the distance of approximately 5km. For each channel we made four simulation setups, two without roughness: Flat

10   no- snow, Flat snow, and two with roughness included: Rough (GO) no-snow, Rough (GO) snow. As for the performance metrics of the model setups, we use the coefficient of determination (r^2), the root-mean-square error (RMSE), the bias and unbiased root- mean-square error (ubRMSE). These metrics are widely used in the assessment of the performance of satellite measurements Entekhabi et al. (2010). Table 1 holds the results of the comparison expressed in terms of r^2, RMSE, bias and ubRMSE. The corresponding scatter-plots illustrating the comparison between measured and modeled brightness temperatures

15   are presented on the Figure 10.

(a) $\theta = 0$, p=H (b) $\theta = 0$, p=V (c) $\theta = 45$, p=H (d) $\theta = 0$, p=V
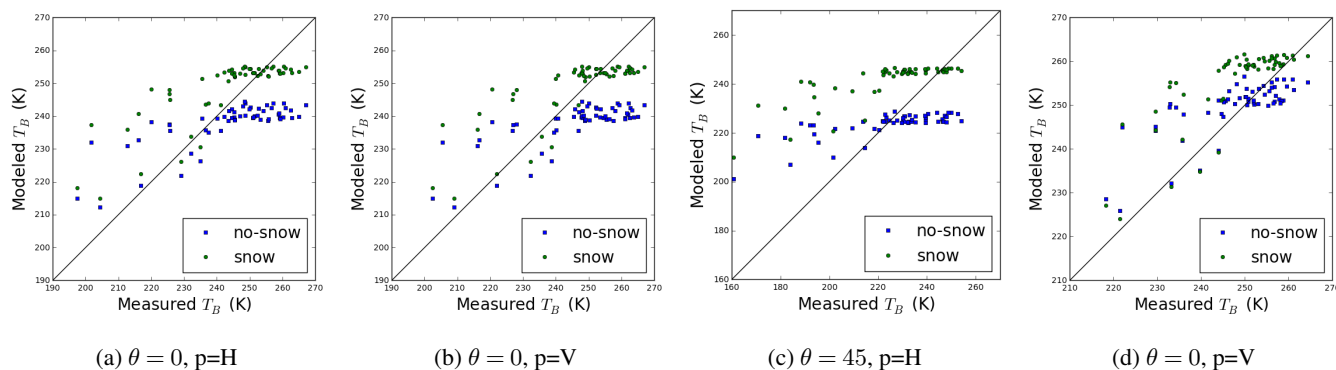
Figure 9. Scatter-plots illustrating the comparisons between the EMIRAD-2 data and the T_B simulated without GO roughness included - **specular**. Results corresponding to the setup with snow are marked in green, without snow in blue.

(a) $\theta = 0$, p=H (b) $\theta = 0$, p=V (c) $\theta = 45$, p=H (d) $\theta = 45$, p=V
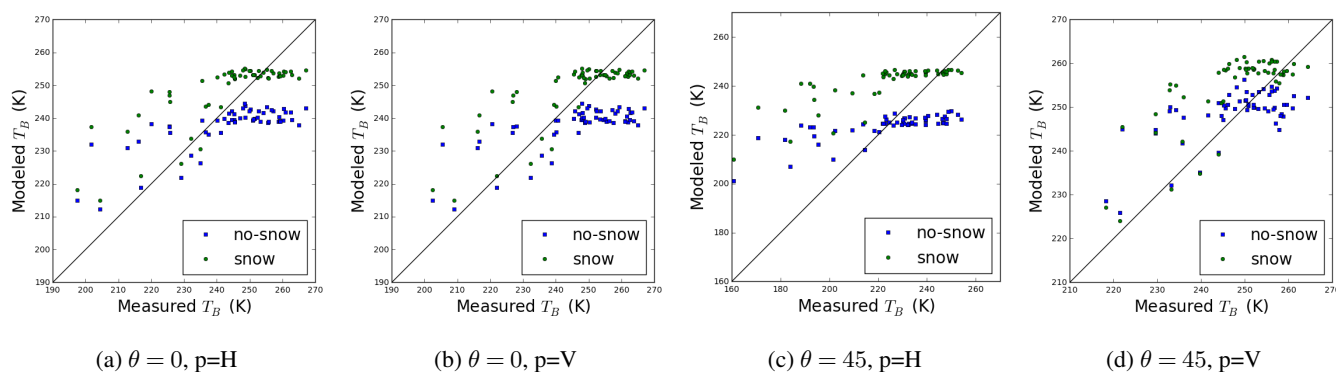
Figure 10. Scatter-plots illustrating the comparisons between the EMIRAD-2 data and the T_B simulated **with GO roughness included**. Results corresponding to the setup with snow are marked in green, without snow in blue.

The values of r^2 for all "channel - simulation setup" combinations do not exceed 0.3. The simplified one-layer model managed to capture only 30% of the signal variance even with surface roughness included. Furthermore, the inclusion of surface roughness brings little improvement to the statistics. In case of vertical polarization, where the model studies indicate the most sensitivity to roughness, the r^2 is even a little lower. The inclusion of a very crude snow thickness parametrization is more successful in capturing the radiometer measurements variability. All metrics show the four model setups perform poorly in reproducing the EMIRAD-2 measurements. The bias is the lowest for the side-looking vertical channel (1.9K to 5K). For the nadir channel the inclusion of snow in the model reduces the bias by 11K to the value of 1.5K. For the horizontal polarization channel the inclusion of snow has an opposite effect, changing the absolute value of bias from 4.5K to -13.2K. The high values of RMSE and ubRMSE show a general miss-fit of the model to the data.

		r^2	RMSE [K]	bias [K]	ubRMSE [K]
T_B, $\theta = 0°$	Flat, no snow	0.21	30.9	12.6	27.8
	Flat, snow	0.29	26.1	1.3	26.7
	Rough, no snow	0.20	30.8	12.5	27.8
	Rough, snow	0.29	26.2	1.5	26.1
$T_B H$, $\theta = 40°$	Flat, no snow	0.22	29.9	4.6	29.5
	Flat, snow	0.30	30.3	-13.2	27.3
	Rough, no snow	0.22	29.8	4.5	29.4
	Rough, snow	0.30	30.3	-13.2	27.3
$T_B V$, $\theta = 40°$	Flat, no snow	0.16	29.1	4.0	28.9
	Flat, snow	0.24	27.2	-1.9	27.1
	Rough, no snow	0.15	29.3	5.0	28.9
	Rough, snow	0.22	27.1	-1.2	27.1

Table 1. Performance of the different T_B simulation setups in terms of coefficient of determination r^2, RMSE [K], bias [K], ubRMSE [K]. For EMIRAD-2 channels four model setups are tested: Flat no snow, Flat snow, Rough no snow, Rough snow. Nadir-looking antenna channels are treated together.

4 Discussion and Conclusions

In this paper we have addressed the issue of the decimetre-scale surface roughness influence on the L band brightness temperature of sea ice. We used the airborne laser scanner (ALS) data to characterize the sea ice surface and to produce the digital elevation model (DEM) of the sea ice surface. From the DEM we derived the probability distribution of surface slopes (α) and their azimuthal orientation (γ). We found that the probability distribution function of α (PDF_α) can be described with an exponential function regardless of the degree of roughness of sea ice surface. The exponent parameter (s_α) is a quasi-quadratic function of the standard deviation of surface heights. In the second part of this work we used the PDF_α in the Monte Carlo simulation of the emission from a faceted sea ice surface. The effect of surface roughness is little noticeable in near-nadir, accounting for up to of 2.6K decrees in T_B . The polarization curves around Brewster's angle are most affected. The vertical polarization is decreased by 8K and horizontal polarization increased by 4K for the roughest ice, compared with the specular sea ice surface. The effect of large-scale surface roughness on polarization curves is not linear with the degree of the surface roughness described by s_α. Meaning that the alteration of the T_B curves is stronger for the roughest surface. The overall

change of emission due to the large-scale surface roughness can be expressed as a superposition of change in intensity (H_α) and an increase in polarization mixing (Q_α). The change in intensity depends primarily on the surface permittivity, whereas the polarization mixing shows little dependence on ϵ. However, the changes in this parameterization are negligible for all types of first-year ice. Lastly, we compared the simulation of the brightness temperature with and without surface roughness with the

5 radiometer measurements. Unfortunately, this had shown that one layer setup of the emission model is not enough to capture the brightness temperature variability at the scale of 60 seconds (5km flight track). The inclusion of surface roughness has proven less important than the inclusion of crude snow thickness parameterization. The possible explanation is that the sea ice in the studied region was highly heterogeneous in term of its permittivity and thickness. Therefore a better result might be obtained if a multi-layer model together with the direct inclusion of sea ice facets orientation in the radiometer field of

10 view was used. This however, would require in-situ measurements of sea ice permittivity, temperature and roughness Thus the author's recommendation for the future studies is to measure the snow and sea ice properties together with surface roughness directly in the radiometer's field of view.

Code and data availability. Code and data are available from the authors at a request.

Author contributions. Conceptualization, M.Miernecki and L.Kaleschke; Methodology, M.Miernecki; Software, M.Miernecki and N.N.Maaß;

15 Validation, M.Miernecki, N.Maaß; Formal Analysis, M.Miernecki and L.Kaleschke; Investigation, M.Miernecki; Resources, L.Kaleschke; Data Curation, S.Hendricks, S.S.Søbjrg; Writing—Original Draft Preparation, M.Miernecki; Writing—Review & Editing, L.Kaleschke, N.Maaß ; Visualization, M.Miernecki; Supervision, L.Kaleschke; Project Administration, L.Kaleschke; Funding Acquisition, L.Kaleschke

This research was funded by the HGF Alliance, Remote Sensing and Earth System Dynamics. The European Space Agency co-financed the AWI research aircraft Polar 5 and helicopter flights (ESA contract 4000110477/14/NL/FF/lf; PI S.Hendricks)

20 and the development and validation of SMOS sea ice thickness retrieval methods (ESA contracts 4000101476/10/NL/CT and 4000112022/14/I-AM; PI L.Kaleschke). Technical University of Denmark (DTU) co-financed and conducted the measurements with EMIRAD2 L-band radiometer on Polar 5.

Competing interests. The authors declare no conflict of interest. The founding sponsors had no role in the design of the study; in the collection, analyses, or interpretation of data; in the writing of the manuscript, and in the decision to publish the results

25 *Acknowledgements.* The authors acknowledge the institutions providing the data and people involved in carrying out the measurements. The TerraSAR-X and TanDEM-X teams provided the SAR data for this study.

The following abbreviations are used in this manuscript:

ALS	airborne Laser Scanner
CDF	Cumulative Distribution Function
DEM	Digital Elevation Model
GO	Geometrical Optics
ITS	Inverse Transform Sampling
MILLAS	MIcrowave L-band LAyered Sea ice emission model
PDF	Probability Distribution Function
RFI	Radio Frequency Interference
SAR	Synthetic Aperture Radar
SMOS	Soil Moisture and Ocean Salinity
T_B	brightness temperature

References

Balling, J. E., Søbjaerg, S. S., Kristensen, S. S., and Skou, N.: RFI detected by kurtosis and polarimetry: Performance comparison based on airborne campaign data, in: 2012 12th Specialist Meeting on Microwave Radiometry and Remote Sensing of the Environment, MicroRad 2012 - Proceedings, 2012.

5 Beckers, J. F., Renner, A. H. H., Spreen, G., Gerland, S., and Haas, C.: Sea-ice surface roughness estimates from airborne laser scanner and laser altimeter observations in Fram Strait and north of Svalbard, Annals of Glaciology, 56, 235–244, https://doi.org/https://doi.org/10.3189/2015AoG69A717, 2015.

Burke, W. J., Schmugge, T., and Paris, J. F.: COMPARISON OF 2. 8- AND 21-cm MICROWAVE RADIOMETER OBSERVATIONS OVER SOILS WITH EMISSION MODEL CALCULATIONS., J Geophys Res, 84, 287–294, https://doi.org/10.1029/JC084iC01p00287, 1979.

10 Choudhury, B. J., Schmugge, T. J., Chang, A., and Newton, R. W.: EFFECT OF SURFACE ROUGHNESS ON THE MICROWAVE EMIS-SION FROM SOILS., Journal of Geophysical Research, 84, 5699–5706, https://doi.org/10.1029/JC084iC09p05699, 1979.

Cox, G. F. N. and Weeks, W. F.: EQUATIONS FOR DETERMINING THE GAS AND BRINE VOLUMES IN SEA ICE SAMPLES., CRREL Report (US Army Cold Regions Research and Engineering Laboratory), 1982.

Devroye, L.: Chapter 4 Nonuniform Random Variate Generation, in: Simulation, edited by Henderson, S. G. and Nelson, B. L., vol. 13 of

15 *Handbooks in Operations Research and Management Science*, p. pp. 83–121, Elsevier, https://doi.org/10.1016/S0927-0507(06)13004-2, 2006.

Dierking, W.: Laser profiling of the ice surface topography during the Winter Weddel Gyre Study 1992, Journal of Geophysical Research, 100, 4807–4820, 1995.

Dierking, W.: RMS slope of exponentially correlated surface roughness for radar applications, IEEE Transactions on Geoscience and Remote

20 Sensing, 38, 1451–1454, https://doi.org/10.1109/36.843040, 2000.

Entekhabi, D., Reichle, H. R., Koster, D. R., and Crow, T. W.: Performance metrics for soil moisture retrievals and application requirements, Journal of Hydrometeorology, 11, 832–840, https://doi.org/http://dx.doi.org/10.1175/2010JHM1223.1, 2010.

Hendricks, S., Steinhage, D., Helm, V., Birnbaum, G., Skou, N., Kristensen, S., Søbjaerg, S., Gerland, S., Spreen, G., Bra-trein, M., and King, J.: SMOSice 2014: Data acquisition report, Tech. rep., https://earth.esa.int/web/guest/campaignsProject:

25 Technicalsupportforthe2014SMOSicecampaigninSESvalbardESAcontractnumber:4000110477/14/NL/FF/lftechnicalreportNo.1,2014, 2014.

Huntemann, M., Heygster, G., Kaleschke, L., Krumpen, T., Mäkynen, M., and Drusch, M.: Empirical sea ice thickness retrieval during the freeze-up period from SMOS high incident angle observations, Cryosphere, 8, 439–451, https://doi.org/10.5194/tc-8-439-2014, 2014.

Kaleschke, L., Tian-Kunze, X., Maaß, N., Beitsch, A., Wernecke, A., Miernecki, M., Müller, G., Fock, B. H., Gierisch, A. M. U., Schlünzen,

30 K. H., Pohlmann, T., Dobrynin, M., Hendricks, S., Asseng, J., Gerdes, R., Jochmann, P., Reimer, N., Holfort, J., Melsheimer, C., Heygster, G., Spreen, G., Gerland, S., King, J., Skou, N., Søbjærg, S. S., Haas, C., Richter, F., and Casal, T.: SMOS sea ice prod-uct: Operational application and validation in the Barents Sea marginal ice zone, Remote Sensing of Environment, 180, 264–273, https://doi.org/http://doi.org/10.1016/j.rse.2016.03.009, 2016.

Ketchum, R.: Airborne laser profiling of the arctic pack ice, Remote Sensing of Environment, 2, 41–52, 1971.

35 Klein, L. and Swift, C.: An improved model for the dielectric constant of sea water at microwave frequencies, IEEE Transactions on Antennas and Propagation, 25, 104–111, https://doi.org/10.1109/TAP.1977.1141539, 1977.

Landy, J., Isleifson, D., Komarov, A., and Barber, D.: Parameterization of Centimeter-Scale Sea Ice Surface Roughness Using Terrestrial LiDAR, Geoscience and Remote Sensing, IEEE Transactions on, 53, 1271–1286, https://doi.org/10.1109/TGRS.2014.2336833, 2015.

Lawrence, H., Demontoux, F., Wigneron, J. P., Paillou, P., Wu, T. D., and Kerr, Y. H.: Evaluation of a Numerical Modeling Approach Based on the Finite-Element Method for Calculating the Rough Surface Scattering and Emission of a Soil Layer, IEEE Geoscience and Remote Sensing Letters, 8, 953–957, https://doi.org/10.1109/LGRS.2011.2131633, 2011.

Lawrence, H., Wigneron, J. ., Demontoux, F., Mialon, A., and Kerr, Y. H.: Evaluating the semiempirical H-Q model used to calculate the L-band emissivity of a rough bare soil, IEEE Transactions on Geoscience and Remote Sensing, 51, 4075–4084, https://doi.org/10.1109/TGRS.2012.2226995, 2013.

Liu, C., Chao, J., Gu, W., Li, L., and Xu, Y.: On the surface roughness characteristics of the land fast sea-ice in the Bohai Sea, Acta Oceanologica Sinica, 33, 97–106, https://doi.org/10.1007/s13131-014-0509-3, 2014.

Maaß, N., Kaleschke, L., Tian-Kunze, X., and Drusch, M.: Snow thickness retrieval over thick Arctic sea ice using SMOS satellite data, Cryosphere, 7, 1971–1989, https://doi.org/10.5194/tc-7-1971-2013, 2013.

Matzler, C. and Standley, A.: Relief effects for passive microwave remote sensing, International Journal of Remote Sensing, 21, 2403–2412, https://doi.org/10.1080/01431160050030538, 2000.

Mironov, V. L., Kerr, Y. H., Kosolapova, L. G., Savin, I. V., and Muzalevskiy, K. V.: A Temperature-Dependent Dielectric Model for Thawed and Frozen Organic Soil at 1.4 GHz, IEEE Journal of Selected Topics in Applied Earth Observations and Remote Sensing, 8, 4470–4477, https://doi.org/10.1109/JSTARS.2015.2442295, 2015.

Mäkynen, M., Cheng, B., and Similä, M.: On the accuracy of thin-ice thickness retrieval using MODIS thermal imagery over Arctic first-year ice, Annals of Glaciology, 54, 87–96, https://doi.org/10.3189/2013AoG62A166, 2013.

Panofsky Hans A. and Brier Glenn W.: Some applications of statistics to meteorology, Pennsylvania State University Press, 1958.

Prigent, C. and Abba, P.: Sea surface equivalent brightness temperature at millimeter wavelengths, Annales Geophysicae [0992-7689], 8, 627–634, 1990.

Ricker, R., Hendricks, S., Helm, V., Skourup, H., and Davidson, M.: Sensitivity of CryoSat-2 Arctic sea-ice freeboard and thickness on radar-waveform interpretation, Cryosphere, 8, 1607–1622, https://doi.org/10.5194/tc-8-1607-2014, 2014.

Søbjaerg, S., Kristensen, S., Balling, J., and Skou, N.: The airborne EMIRAD L-band radiometer system, pp. 1900–1903, https://doi.org/10.1109/IGARSS.2013.6723175, 2013.

Stroeve, J. C., Markus, T., Maslanik, J. A., Cavalieri, D. J., Gasiewski, A. J., Heinrichs, J. F., Holmgren, J., Perovich, D. K., and Sturm, M.: Impact of surface roughness on AMSR-E sea ice products, IEEE Transactions on Geoscience and Remote Sensing, 44, 3103–3116, https://doi.org/10.1109/TGRS.2006.880619, 2006.

Strübing, K. and Schwarz, J.: Die Eisverhältnisse in der Barentssee während der IRO-2-Testfahrt mit R/V Lance 17. – 27.03.2014, Tech. rep., abschlussbericht vorgelegt von JS Consulting, Großhansdorf, im Auftrag des AWI, Bestellnummer 12/45086354 zum Werkvertrag Vor -/Nachbereitung und Durchführung der IRO-2-Testfahrt im Rahmen des Vorhabens Entwicklung und Optimierung eines Ozean-Meereis Vorhersagemodells für das Nordpolarmeer, BMWi-Förderkennzeichen: 03SX328H, 2014.

Tian-Kunze, X., Kaleschke, L., Maaß, N., Mäkynen, M., Serra, N., Drusch, M., and Krumpen, T.: SMOS-derived thin sea ice thickness: Algorithm baseline, product specifications and initial verification, Cryosphere, 8, 997–1018, https://doi.org/10.5194/tc-8-997-2014, 2014.

Tiuri, M. E., Sihvola, A. H., Nyfors, E. G., and Hallikaiken, M. T.: The Complex Dielectric Constant of Snow at Microwave Frequencies, IEEE Journal of Oceanic Engineering, 9, 377–382, https://doi.org/10.1109/JOE.1984.1145645, 1984.

Ulaby, F. T., Long, D. G., Blackwell, W. J., Elachi, C., Fung, A. K., Ruf, C., Sarabandi, K., Zebker, H. A., and Van Zyl, J.: Microwave radar and radiometric remote sensing, University of Michigan Press Ann Arbor, 2014.

Untersteiner, N.: On the mass and heat budget of arctic sea ice, Archiv für Meteorologie, Geophysik und Bioklimatologie Serie A, 12, 151–182, 1961.

5 Vant, M. R., Ramseier, R. O., and Makios, V.: The complex-dielectric constant of sea ice at frequencies in the range 0.1-40 GHz, Journal of Applied Physics, 49, 1264–1280, 1978.

Warren, S. G., Rigor, I. G., Untersteiner, N., Radionov, V. F., Bryazgin, N. N., Aleksandrov, Y. I., and Colony, R.: Snow depth on Arctic sea ice, Journal of Climate, 12, 1814–1829, https://doi.org/10.1175/1520-0442(1999)012<1814:SDOASI>2.0.CO;2, 1999.

Yu, Y. and Rothrock, D. A.: Thin ice thickness from satellite thermal imagery, Journal of Geophysical Research C: Oceans, 101, 25753–
10 25766, https://doi.org/10.1029/96JC02242, 1996.